AZIMUTHAL ANISOTROPY INVESTIGATIONS FOR P AND S WAVES: A PHYSICAL MODELLING EXPERIMENT

Khaled Al Dulaijan, Gary F. Margrave, and Joe Wong

ABSTRACT

Information related to fracture orientation and intensity is vital for the development of unconventional hydrocarbons, such as tight sand gas and shale gas. Numerical modeling provides a valuable tool for geophysicists to test and validate their methodologies that provide them with information about reservoirs. Fractures make numerical modeling more complicated and introduce complexities that might even require geophysicists to validate their numerical models before using them to assess their methods. Alternatively, physical modeling provides a unique opportunity to test, validate, and develop methods for characterizing fractured reservoirs. This report utilizes seismic physical modeling for fracture characterization.

A two-layer model was built using vertically laminated Phenolic overlain by Plexiglas to represent a fractured reservoir overlaid by an isotropic overburden. The first dataset was acquired over that 2-layer model and consist of three 9-component common-receivers. P-wave first-arrival times were analyzed on all three gathers and fracture orientation was predicted. An Alford rotation was applied to the four horizontal components and successfully minimized energy on components other than those two that are related to the fast S wave and slow S wave. However, the angle between natural and acquisition coordinate systems was not predicted correctly. One possible reason could be the contact between the two media. Therefore, another dataset was acquired using a single Phenolic layer. Alford rotation was applied and the angle between natural and acquisition coordinate system was predicted correctly. That dataset was used too to measure the stiffness coefficients tensor using group velocity data.

INTRODUCTION

Understanding fracture orientation and intensity is often challenging, yet important for the optimal development of fractured reservoirs. Fractures can act as conduits for fluid flow. Seismic anisotropy can assist in understanding fractures, even though it may be related to fine layering or particle alignment. In this report, we are interested in fracture-induced seismic anisotropy, and more specifically in vertical fractures. Azimuthal anisotropy (i.e. Horizontal-Transverse Isotropy (HTI) or Orthorhombic Anisotropy) can be related to vertical fractures. Azimuthal anisotropy makes numerical modeling hard and introduces uncertainties. On the other hand, physical modeling provides a reliable alternative. This report is a continuation to previous CREWES work (e.g. Wong et al., 2012; Mahmoudian 2013; Mahmoudian and Margrave 2013) that utilizes physical modeling.

In the physical modeling laboratory, a fractured reservoir and isotropic overburden can be represented by two layers: one anisotropic and one isotropic. Because azimuthal anisotropy is of interest to us, we want to acquire gathers of common offset and varying azimuthal angles. In such a way, fracture orientation can be predicted from azimuthal analysis of P-wave first arrival times. Also, it can be predicted by S-wave splitting because fast S wave polarization direction indicates directly the orientation of fractures (Winterstein, 1994). Regularly, a four-component horizontal rotation (i.e. Alford rotation) is needed to separate the fast S wave from the slow S wave. Azimuthal common-offset receiver gathers have wide range of azimuth angles but limited range of angle of incidence. Shots are distributed along a circle covering 360^o azimuth. Therefore, they are ideal for Horizontally-Transverse Isotropy (HTI) media. In this study, common azimuth shot gathers were also collected and analyzed. Such gathers are ideal for Vertically-Transverse Isotropy (VTI) media. Two data sets were acquired over different models for this report:

1. Three circular common-receiver gathers with radii equal to 250 m, 500 m and 1000 m were acquired over a 2-layer model. In that dataset, a 3-C receiver and a 3-C source yield produce 9-C receiver gathers.

2. One circular gather, which has a 200 m radius, and two linear gathers with 0^o and 90^o azimuths were acquired over the anisotropic medium. In that dataset, a 3-C receiver and a 2-C horizontal source resulted in 6-C shot gathers.

Alford rotation analysis was the motivation for acquiring the second dataset because results of the first dataset for the rotational analysis were not as predicted from the physical model.

SEISMIC ANISOTROPY

Suppose that we throw a stone into a swimming pool. A wave will originate when and where the stone hits the water surface. The wave will travel along all directions at the same speed. As a result, the outer circle, or the wavefront, will have a circular shape. This property (velocity being same in all directions) of the wave is called isotropy. On the other hand, the dependence of velocity on direction is called anisotropy. In the anisotropic case, the wavefront does not form a circle (or a sphere in 3D), as shown in Figure 1. The group velocity ($\vec{g}$) of the wave, at point A, is the ratio of distance between the origin and A divided by the time that took the wave to travel that distance. Note that the group velocity is not normal to the wavefront, as shown by Figure 1. The phase velocity ($\vec{v}$) is normal to the wavefront and it measures the velocity of single frequency (Vestrum, 1994).

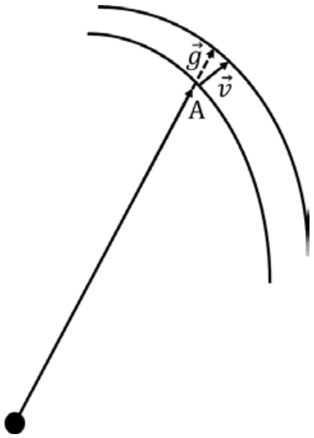

Fig. 1. Wavefront of seismic waves in an anisotropic medium. Note that it does not form a circle. $\vec{g}$ measures the distance between the source and the wavefront divided by the traveltime. $\vec{v}$ is perpendicular to the wavefront (modified after Vestrum 1994).

Stiffness coefficients are used to describe anisotropy. Stiffness relates stress to the strain in the following manner:

$$\sigma_{ij} = c_{ijkl}\epsilon_{kl} \, , \tag{1}$$

where *i*, *j*, *k*, and *l* are 1, 2, and 3. σ_{ij} is the second-order stress tensor, c_{ijkl} is the fourth order stiffness tensor, and ϵ_{kl} is the second order strain tensor. The stress and strain tensors have 9 (3x3) element each, while the stiffness tensor has 81 elements. In the unit cube, shown in Figure 2, σ_{ij} defines the stress exerted on the *i* face along the *j* direction. Similarly, ϵ_{kl} defines the stress exerted on the k face along the l direction. Because of symmetry, stress elements σ_{ij} and σ_{ji} are equal (i.e. $\sigma_{32} = \sigma_{23}$). Therefore, the stress tensor is reduced to 6 elements. Similarly, the strain tensor is reduced to 6 elements. From the symmetry of the stress and strain,

$$c_{ijkl} = c_{jikl}, \tag{2}$$

and

$$c_{ijkl} = c_{ijlk}. \tag{3}$$

Therefore, the stiffness tensor is reduced to 36 elements. For simplicity, the stiffness tensor is represented in the Voigt notation, such that 11 is 1, 22 is 2, 33 is 3, 32 and 23 are 4, 31 and 13 are 5, 21 and 12 are 6. The fourth order tensor c_{ijkl} is represented by a second order tensor C_{ij}, where *i* and *j* are 1, 2, …, 6 (Thomsen, 1986).

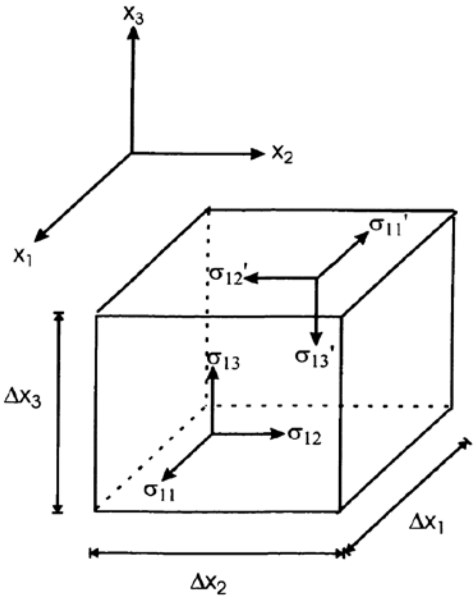

Fig. 2. Components of stress tensor. σ_{ij} defines the stress exerted on the *i* face along the *j* direction (after Mah 1999)

Isotropic media has only two independent elements in the stiffness coefficient tensor (C_{ij}) which can be written in terms of Lamé parameters (λ and μ) (Musgrave 1970)

$$\mathrm{C}_{\mathrm{ij}} = \begin{bmatrix} \lambda+2\mu & \lambda & \lambda & 0 & 0 & 0 \\ \lambda & \lambda+2\mu & \lambda & 0 & 0 & 0 \\ \lambda & \lambda & \lambda+2\mu & 0 & 0 & 0 \\ 0 & 0 & 0 & \mu & 0 & 0 \\ 0 & 0 & 0 & 0 & \mu & 0 \\ 0 & 0 & 0 & 0 & 0 & \mu \end{bmatrix} \tag{4}$$

Anisotropy can be classified according to symmetry. Transverse isotropy (TI) is the most simple and most commonly used type of anisotropy by geophysicists. In transverse isotropy, there is one axis of symmetry. Stiffness coefficient tensor can be characterized by five independent elements. Transverse isotropy is classified into: Vertically-Transverse Isotropy (VTI), Horizontally-Transverse Isotropy (HTI), and Tilted-Transverse Isotropy (TTI). Figure 3 (top) shows the two types of TI symmetry: HTI and VTI. Another classification of anisotropy, which is often used by geophysicists, is orthorhombic symmetry. Orthorhombic media have three orthogonal planes of symmetry, as shown by Figure 3 (bottom). The density-normalized stiffness coefficient tensor ($\mathrm{A}_{\mathrm{ij}} = C_{ij} / \rho$; where ρ is density) for an orthorhombic media has nine independent elements;

$$A_{ij} = \begin{bmatrix} A_{11} & A_{12} & A_{13} & 0 & 0 & 0 \\ A_{12} & A_{22} & A_{23} & 0 & 0 & 0 \\ A_{13} & A_{23} & A_{33} & 0 & 0 & 0 \\ 0 & 0 & 0 & A_{44} & 0 & 0 \\ 0 & 0 & 0 & 0 & A_{55} & 0 \\ 0 & 0 & 0 & 0 & 0 & A_{66} \end{bmatrix} \tag{5}$$

(Vestrum, 1994) or (Mahmoudian et al., 2014). There are other types of symmetry, such as cubic or monoclinic, that geophysicists rarely use.

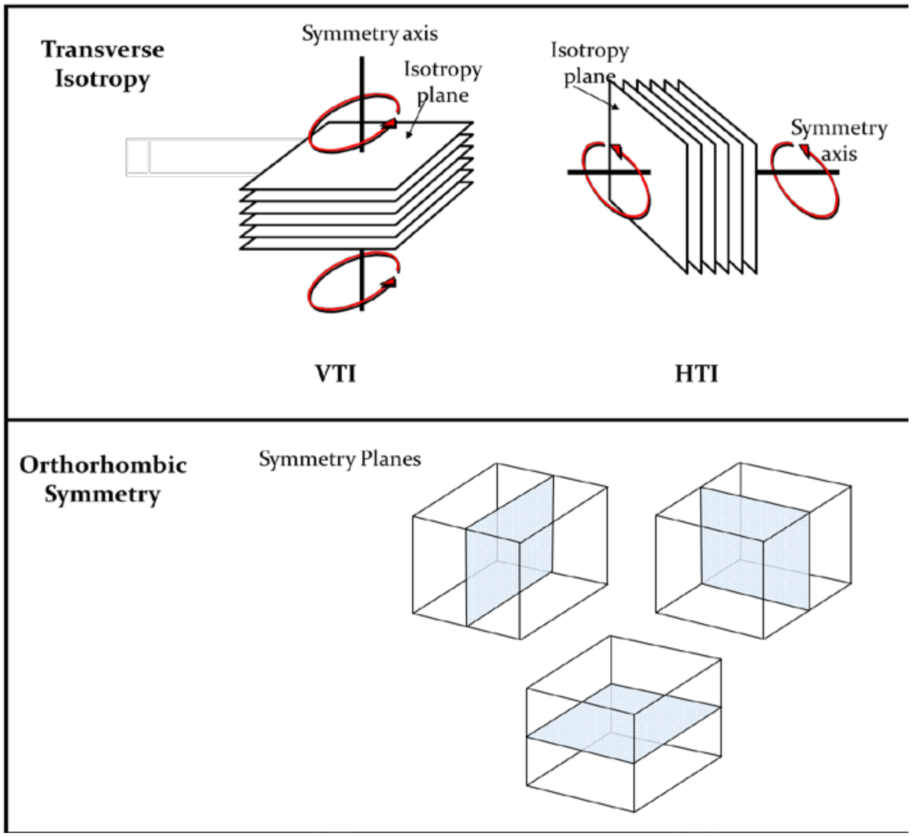

Fig. 3. Transverse Isotropy (top): two types of transverse isotropy are displayed. VTI has vertical symmetry axis and HTI has horizontal symmetry axis. Orthorhombic Symmetry (bottom): three orthogonal planes of symmetry.

PHYSICAL MODELING

A physical model was constructed to represent a vertically fractured reservoir overlain by isotropic overburden, as shown in Figure 4. The vertically fractured reservoir exhibits an HTI type anisotropy, or more precisely, slightly orthorhombic anisotropy (Mahmoudian, 2013). For VTI or HTI anisotropy, Phenolic material can be used. Vertically laminated sheets of linen fabric bonded with Phenolic resin compose the Phenolic HTI medium (Figure 5).

FIG. 4. A physical model consisting of a Phenolic layer under a Plexiglas layer, and representing a fractured reservoir overlain by isotropic overburden. Laboratory to field scale is 1:10,000 in both length and time. Scaled thicknesses of Plexiglas and Phenolic layers are 480 m and 450 m respectively.

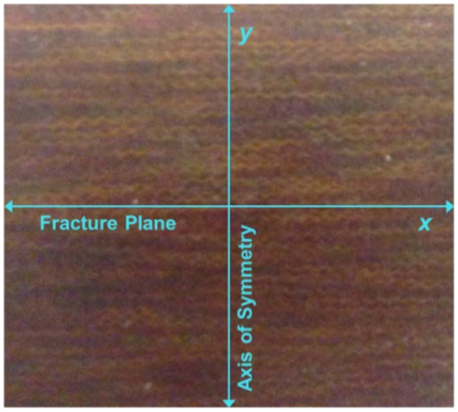

FIG. 5. An expanded view of laminated Phenolic layer. Lamination direction is along the x-axis and represents the reservoir fracture plane. Axis of symmetry is along the y-axis.

In the Phenolic medium, the P wave is fastest (3570 m/s) along the vertical laminations, slowest (2900 m/s) perpendicular to the vertical lamination, and somewhere in between along other directions. On the other hand, the S wave is fastest (1700 m/s) along the vertical laminations, slowest (1520 m/s) perpendicular to the vertical lamination, and undergoes S-wave splitting in other directions. The isotropic overburden was obtained by introducing Plexiglas. P-wave and S-wave velocities in the isotropic medium are 2745 m/s and 1520 m/s respectively. Properties of Phenolic and Plexiglas are summarized in Table 1 (Mahmoudian, 2013).

	P-wave velocity (m/s)	S-wave velocity (m/s)	Density (g/cc)
Plexiglas	2745	1380	1.19
Phenolic	3570/2900	1700/1520	1.39

Table 1. Velocities and densities of Plexiglas and Phenolic.

As previously mentioned, the laboratory to field scale is 1:10,000 in both length and time. Scaled thicknesses of Plexiglas and Phenolic layers are 480 m and 450 m respectively. The acquisition layout for the first dataset is illustrated in Figure 6. Three common-receiver gathers were acquired. One receiver location was fixed at the bottom of the Phenolic layer and centered at the middle of its surface. For each common-receiver gather, 90 source locations were distributed along a circle of radius (***r***) and separated by 4°. Three receiver gathers were acquired with ***r*** = 250 m, 500 m and 1000 m. 3-C receiver and 3-C source yield into 9-component receiver gathers. For the second dataset, one circular gather which has 200 m radius and two linear gathers with 0° and 90° azimuths were acquired over the Phenolic medium. 3-C receiver and 3-C source resulted in 9-component receiver gathers. 3-C receiver and 2-C horizontal source produced 6-component shot gathers. The acquisition layout of the second dataset is described in Figure 7.

Contact transducers were used as P-wave and S-wave sources and receivers. P-wave transducers have a central frequency at 2.38 MHz, while S-wave transducers have central frequency at 5.82 MHz At each station (source/receiver), three transducers were used; one for the vertical component and two for the horizontal components along x- and y-axes. Source and receiver transducers were positioned with a robotic system that has an error of less than 0.1 mm in laboratory scale.

P-WAVE FIRST-ARRIVAL TIMES ANALYSIS

Three common-receiver gathers at r = 250 m, 500 m and 1000 m are shown in Figures 8-10. Each gather (v_{ij}) is composed of 9 components. The first subscript of v denotes the receiver component, while the second subscript denotes the source component. The x-, y-, and z-components are labeled by the numbers 1, 2, and 3 respectively. For example, v_{31} was acquired with a vertical receiver due to a source along the x-axis.

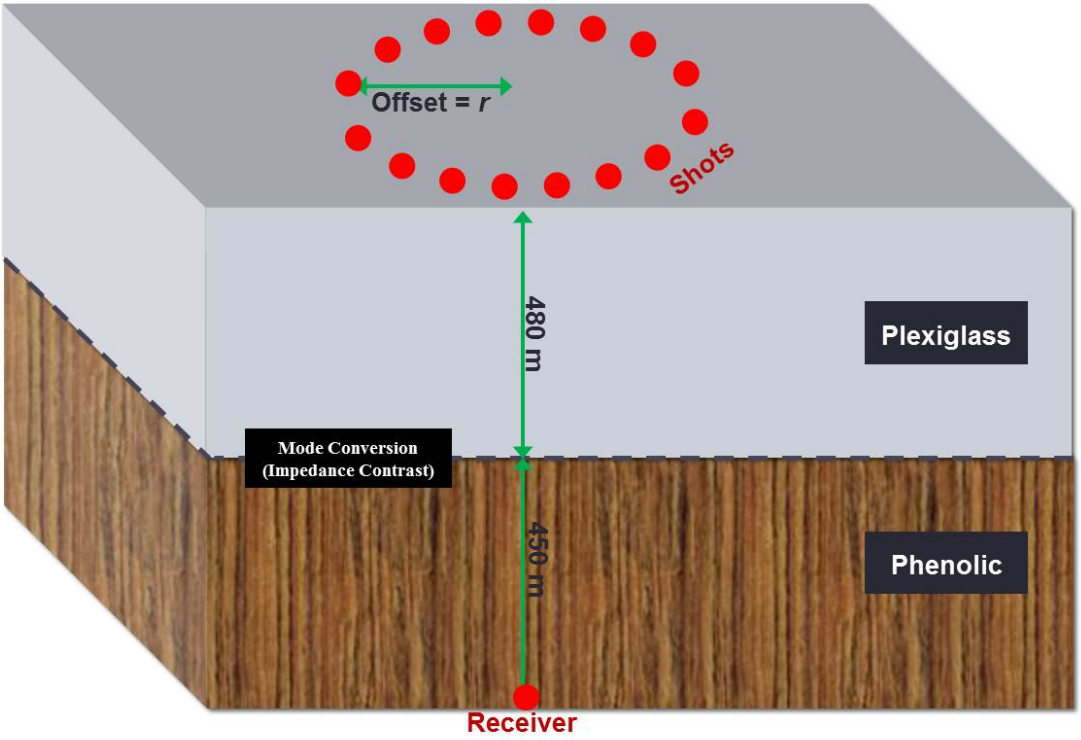

FIG. 6. Acquisition layout for first dataset. One receiver is located at the bottom of the Phenolic layer and centered at the middle of its surface. 90 shot locations are distributed along a circle of radius (***r***) and separated by 4^o. Three receiver gathers are acquired with r = 250 m, 500 m and 1000 m. 3-C receiver and 3-C source yield 9-C receiver gathers.

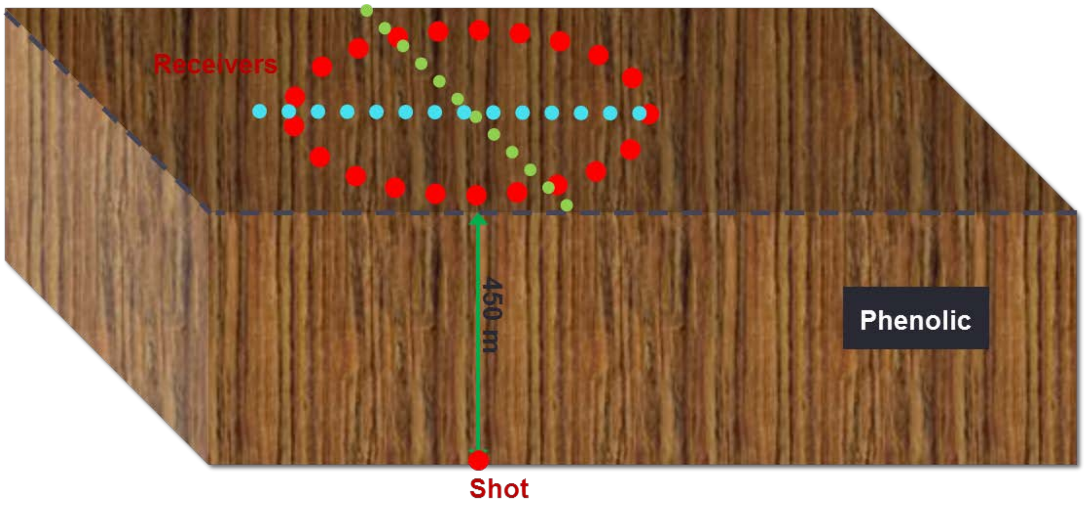

FIG. 7. Acquisition layout for second dataset. One shot is located at the bottom of the Phenolic layer and centered at the middle of its surface. For the first common-shot gather, 90 receiver locations are distributed along a circle of radius equal to 200 m (field scale) and separated by 4^o. Receivers are distrubuted along a line with azimuth equal to 0^o (indicated by blue circles) and 90^o (indicated by green circles)for the seond and third common-shot gathers respectively. 3-C receiver and 2-C horizontal source yield 6-C shot gathers.

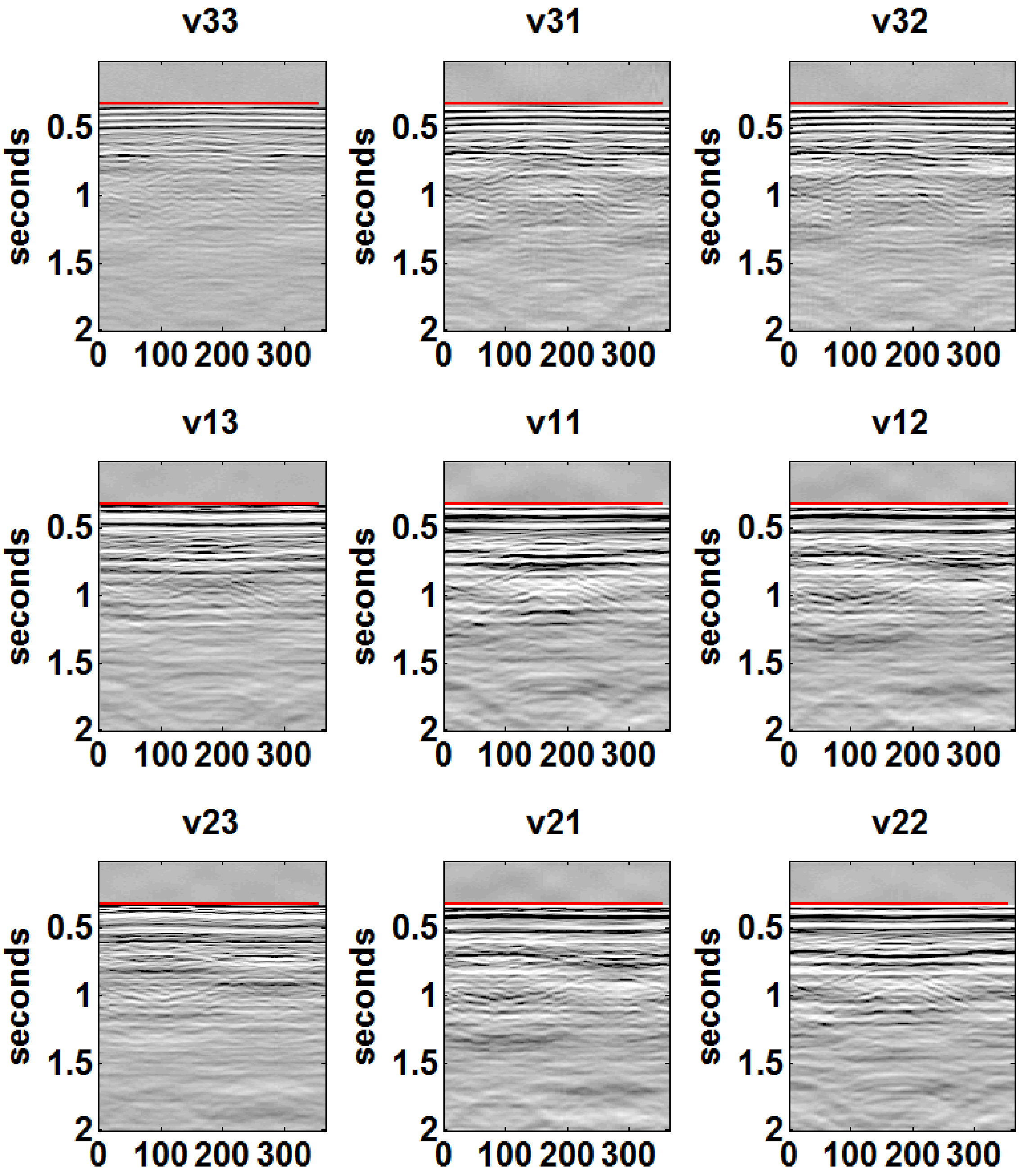

FIG. 8. 9-C receiver gather with ***r*** = 250 m. P-wave first arrival times are indicated by red. The horizontal axis is the azimuth angles which go from 0º to 360º with a 4º increment.

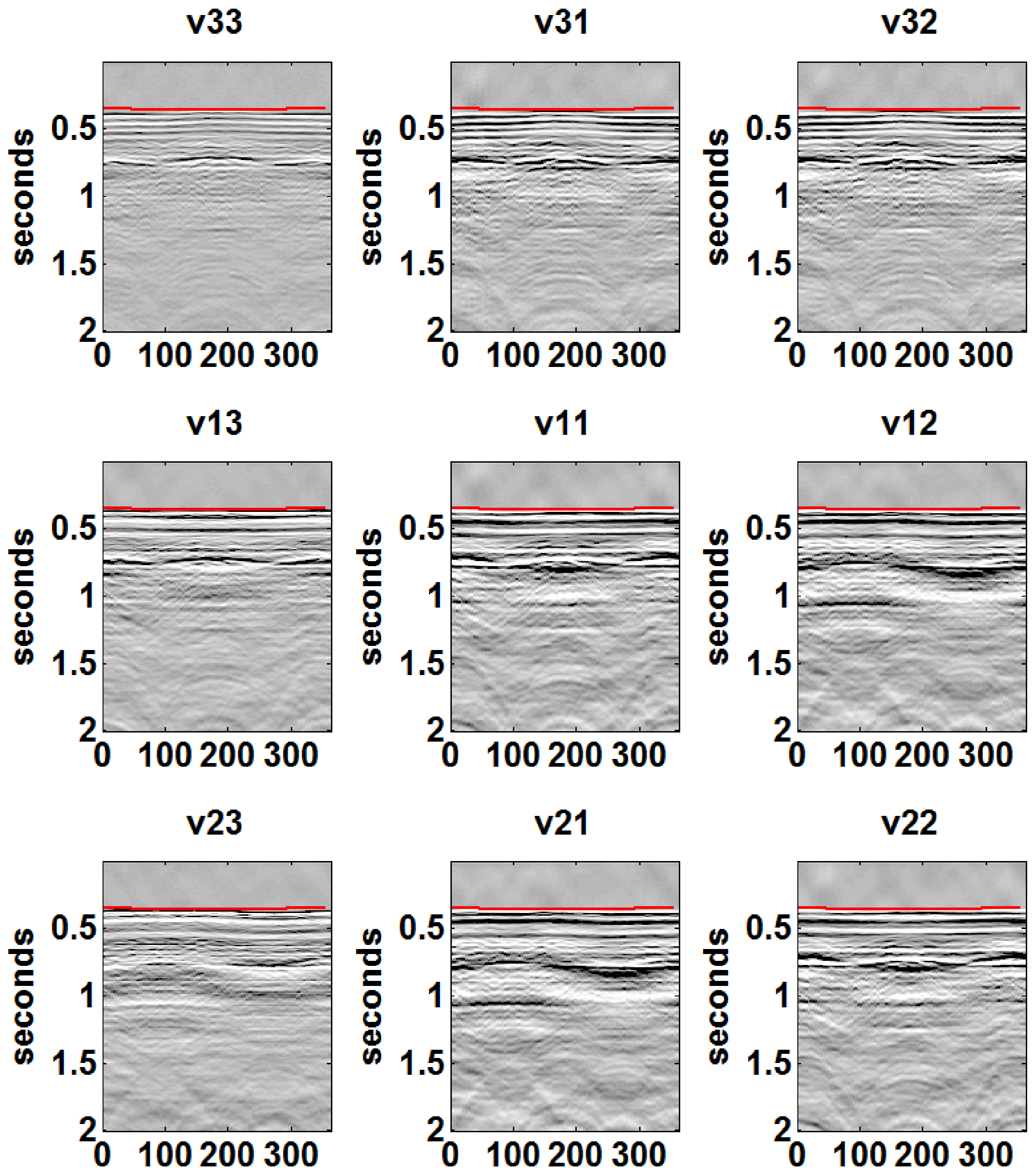

FIG. 9. 9-C receiver gather with r = 500 m. P-wave first arrival times are indicated by red. The horizontal axis is the azimuth angles which go from 0o to 360o with a 4o increment.

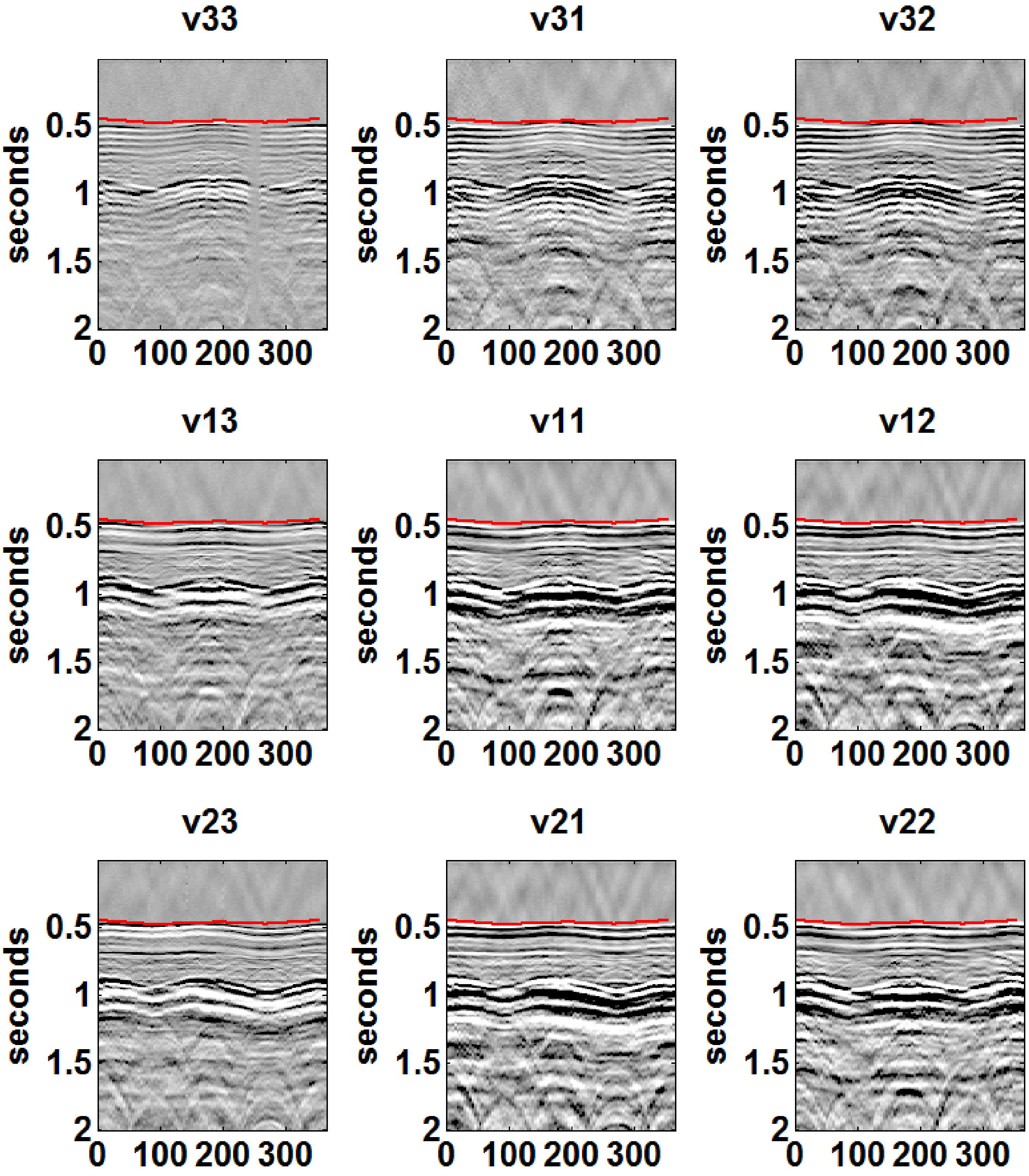

FIG. 10. 9-C receiver gather with ***r*** = 1000 m. P-wave first arrival times are indicated by red. The horizontal axis is the azimuth angles which go from 0° to 360° with a 4° increment.

The three common-receiver gathers in Figures 8-10 are plotted with the same amplitude range. Azimuth varies from 0° to 360° with an increment of 4° for the 1st to the 90th trace. First arrival times were picked on first onset and indicated by red. The 250-m and 500-m common-receiver gathers show nearly constant first-arrival times with increasing azimuth angle. The 1000-m common-receiver gather show a sinusoidal variation of first arrival times with increasing azimuth angle. The acquisition layout suggests that components $\boldsymbol{v}_{11}$ of the three gathers in Figures 8-10 are acquired with horizontal receivers and sources whose polorziation directions are along the x-axis (or parallel to fracture plane). Similarly, $\boldsymbol{v}_{22}$ components have transducer polarization perpendicular to fracture plane.

In isotropic media, P-wave first-arrival times are constant for the same offset and different azimuths. Each common-receiver gather in Figures 8-10 has a constant offset. Figure 10 shows first-arrival times that are variant with azimuth angle and look like a sinusoidal function. Early first arrivals are at 0^o, 180^0, and 360^0. Those angles define the fast P-wave direction which is parallel to the fracture plane. This result is in agreement with the physical model where fracture plane within the Phenolic is along $\boldsymbol{x}$-axis, as can be seen by Figure 2. In Figures 8 and 9, it is hard to see sinusoidal first-arrival times.

If plotted azimuthally in a polar view, sinusoidal first-arrival times appear as an ellipse. The minor axis of the ellipse indicates early first-arrival times, while the major axis indicates late first-arrival times. Therefore, the minor axis indicates the fracture plane (Al Dulaijan et al., 2012).

For each common-receiver gather, first-arrival times are plotted azimuthally in a polar view. Then by least-squares fitting, an ellipse is fitted. Figures 11-13 show elliptical fitting of first-arrival times for each gather. The minor axis for the first and second gather (Figures 12 and 13) is at 5^o. The minor axis for the third gather is 1^o (Figure 13). The minor axes indicate the fracture plane which is supposed to be 0^o according to the physical model (Figure 5). The first and second common-receiver gathers have a smaller offset than the third gather, and therefore are more sensitive to acquisition inaccuracies.

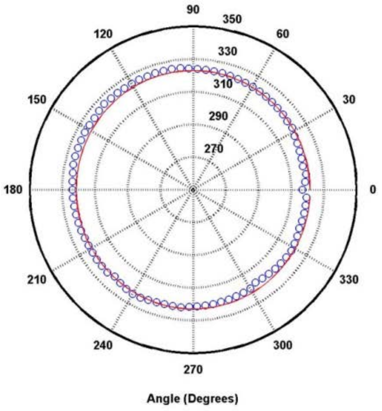

FIG. 11. Elliptical fitting of first-arrival times for the first receiver gather ($\boldsymbol{r}$ = 250 m). The minor axis is at 5^0.

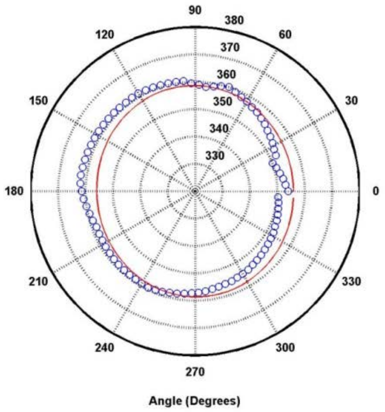

FIG. 12. Elliptical fitting of first-arrival times for the second receiver gather (***r*** = 500 m). The minor axis is at 5^0.

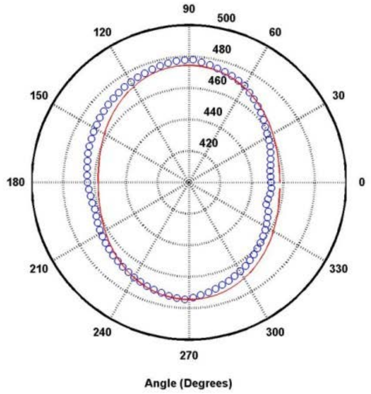

FIG. 13. Elliptical fitting of first-arrival times for the third receiver gather (***r*** = 1,000 m). The minor axis is at 1^0.

S-WAVE SPLITTING: ALFORD ROTATION

In the HTI media, the P wave is fastest along the fracture planes, slowest perpendicular to fracture planes, somewhere in between in other direction. On the other hand, S wave has to split into two phases; a phenomena known as S-wave splitting, S-wave birefringence, or S-wave double-refraction. Polarizations of the two S waves are determined by anisotropy axis of symmetry. The fast S is polarized along the fracture planes and slow S is perpendicular to the fracture planes. Beside the anisotropy axis of symmetry, the velocity of S wave is controlled also by the angle of incidence and the azimuth of propagation. The two S waves travel at different velocities (within the Phenolic) and are recorded at different times. The delay in time is proportionally related to the degree of S-wave anisotropy and thickness of the anisotropic medium (Crampin, 1981).

For all three common-receiver gathers, horizontal components of receivers and sources were aligned along $\boldsymbol{x}$- or $\boldsymbol{y}$-axis. In other words, they were aligned either parallel to fracture plane or normal to the fracture plane. In such a way, S wave is fast along $\boldsymbol{y}$-axis and slow along $\boldsymbol{x}$-axis. In other directions, S wave undergoes S-wave splitting and repolarizes along fast and slow directions. Fast S wave should mostly be recorded by $\boldsymbol{v}_{11}$ and slow S wave by $\boldsymbol{v}_{22}$. Energy on $\boldsymbol{v}_{12}$ and $\boldsymbol{v}_{21}$ should be minimal. This was not the case in our experiment! That suggests an error in the polarization direction of the horizontal transducers.

An Alford 4-component rotation (Alford, 1986) can be used to statistically rotate horizontal components ($\boldsymbol{V}$) recorded in acquisition recorded system into anisotropy natural coordinate system ($\boldsymbol{U}$) using rotation matrix ($\boldsymbol{R}(\theta)$):

$$V = \begin{bmatrix} v_{11} & v_{12} \\ v_{21} & v_{22} \end{bmatrix}, \tag{6}$$

$$U = \begin{bmatrix} u_{11} & u_{12} \\ u_{21} & u_{22} \end{bmatrix}, \tag{7}$$

and

$$R(\theta) = \begin{bmatrix} \cos\theta & sin\theta \\ -sin\theta & cos\theta \end{bmatrix} \tag{8}$$

The rotation matrix, $\boldsymbol{R}(\theta)$ is an orthogonal matrix that gives the identity matrix when multiplied by its transpose or its inverse. To find a new basis of the natural coordinate system, the counterclockwise rotation by angle (θ) is

$$U = R(\theta)\, V\, R^T(\theta). \tag{9}$$

Substituting equations (6), (7), and (8) into equation (9):

$$\begin{bmatrix} u_{11} & u_{12} \\ u_{21} & u_{22} \end{bmatrix} =$$

$$\begin{bmatrix} \cos^2\theta\, v_{11} + \sin^2\theta\, v_{22} + 0.5\sin 2\theta\,(v_{21} + v_{12}) & \cos^2\theta\, v_{12} - \sin^2\theta\, v_{21} + 0.5\sin 2\theta\,(v_{22} - v_{11}) \\ \cos^2\theta\, v_{21} - \sin^2\theta\, v_{12} + 0.5\sin 2\theta\,(v_{22} - v_{11}) & \cos^2\theta\, v_{22} + \sin^2\theta\, v_{11} - 0.5\sin 2\theta\,(v_{21} - v_{12}) \end{bmatrix}. \tag{10}$$

Equation (10) transforms $\boldsymbol{V}$, horizontal components in acquisition coordinate system into the natural coordinate system (Alford, 1986).

The rotation angle (θ) is found by scanning different angle values, and then selecting the angle that minimizes u_{12} and/or u_{21}. For each common-receive gather, angles were scanned within a time window to determine the rotation angle (θ) and Alford rotation was applied. Four horizontal components of the 1st common-receiver gather for r = 250 m is shown before rotation on the left of Figure 14 and after rotation on the right of the same figure. Figure 15 shows the cross energy of different rotation angles. For this common-receiver gather, the rotation angle (θ) is 45^o. Alford rotation was applied to the other two common-receiver gathers. All three gathers acquired over the 2-layer model have rotation angles around 45^o. Ideally, Alford rotation is not needed for this dataset because the acquisition and natural system coordinate are identical. However, this was not the case. One possible reason may be the contact between the Plexiglas and the Phenolic or lack thereof. Therefore, the second dataset was acquired over the Phenolic medium only. The second dataset consists of one circular gather which has 200 m radius and two linear gathers with 0^o and 90^o azimuths, as shown by Figure 7. Alford rotation was applied to the second dataset as well. Figures 16, 18, and 20 show the unrotated data and the rotated data of the second dataset that was acquired over the Phenolic medium. The cross energy of the three common-shot gathers, belonging to the first dataset, are shown in Figures 17, 19, and 21.

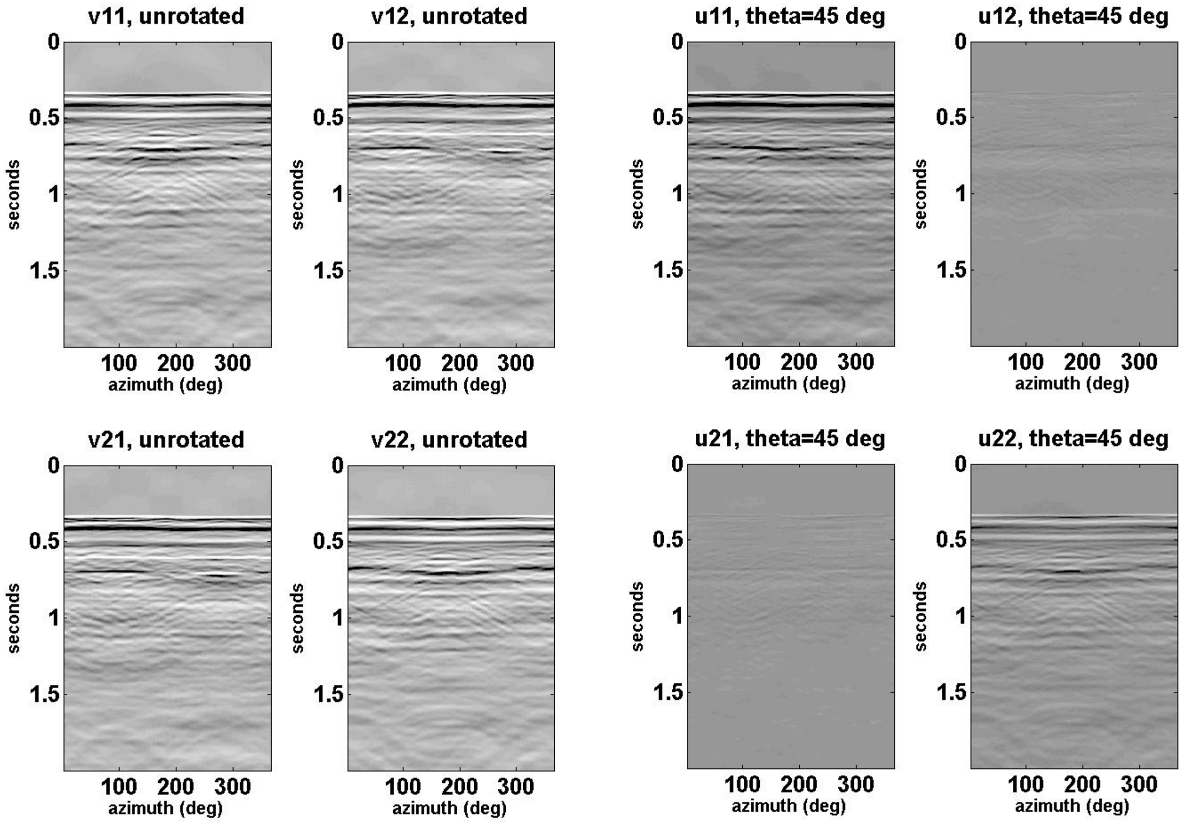

FIG. 14. 250-m circular receiver gather acquired over the 2-layer model: 4 Horizontal components before rotation (left) and after rotation (right).

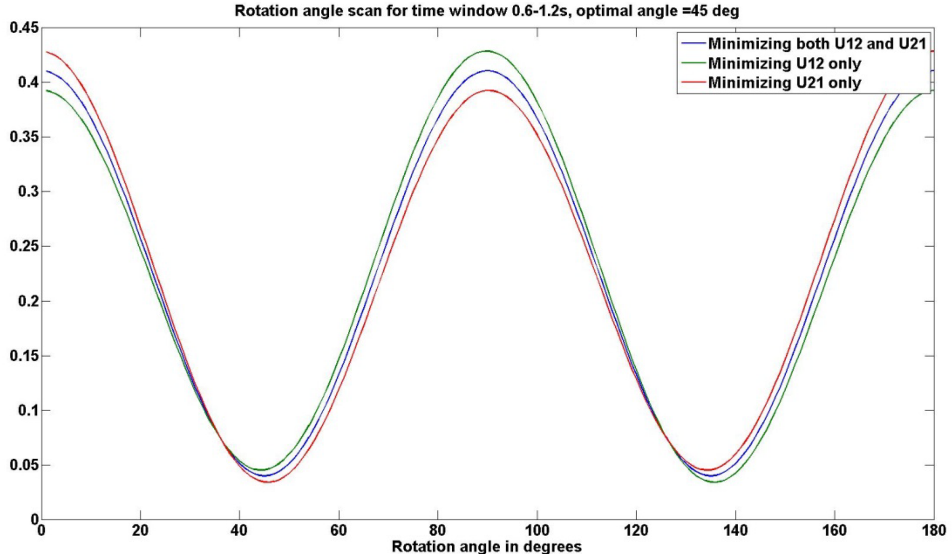

FIG. 15. 250-m circular receiver gather: cross energy vs. rotation angle.

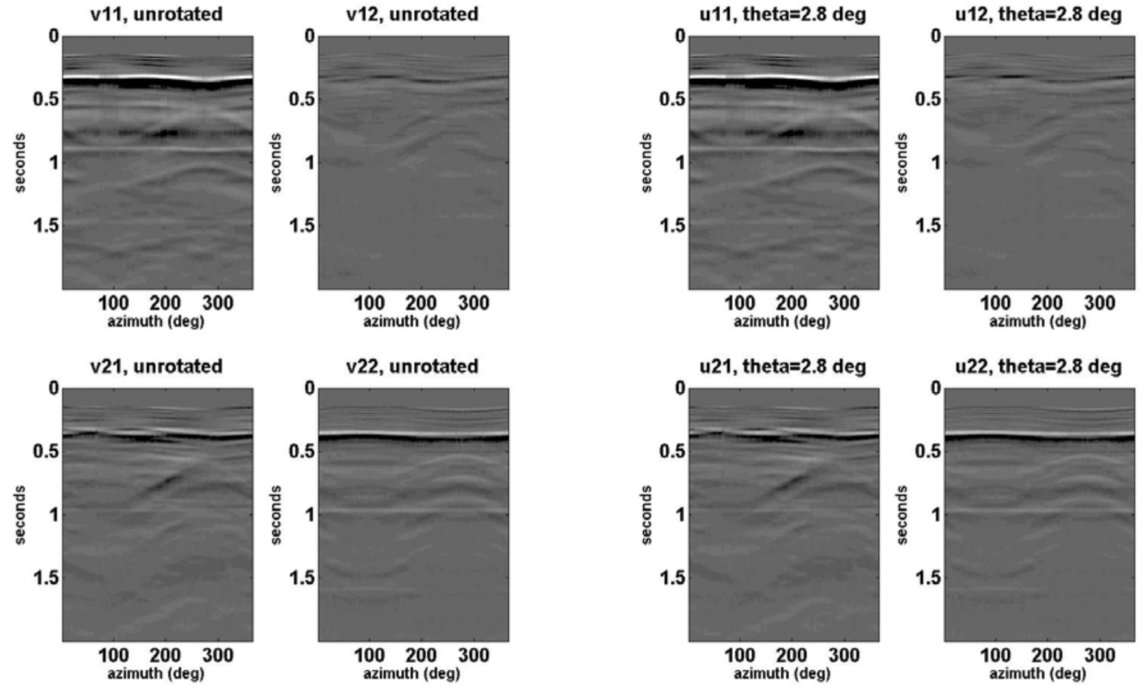

Fig. 16. 200-m circular shot gather acquired over the Phenolic layer: 4 Horizontal components before rotation (left) and after rotation (right).

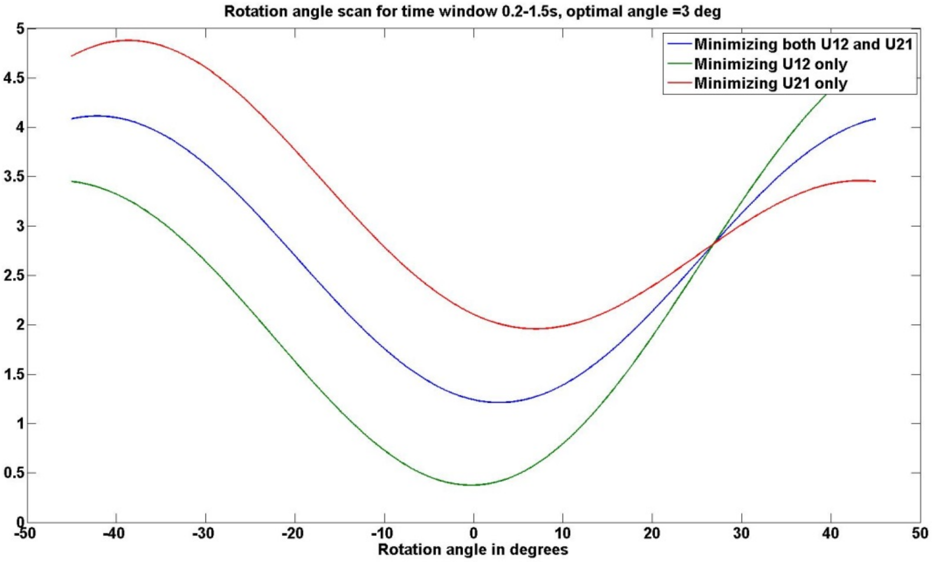

FIG. 17. 200-m circular shot gather: cross energy vs. rotation angle.

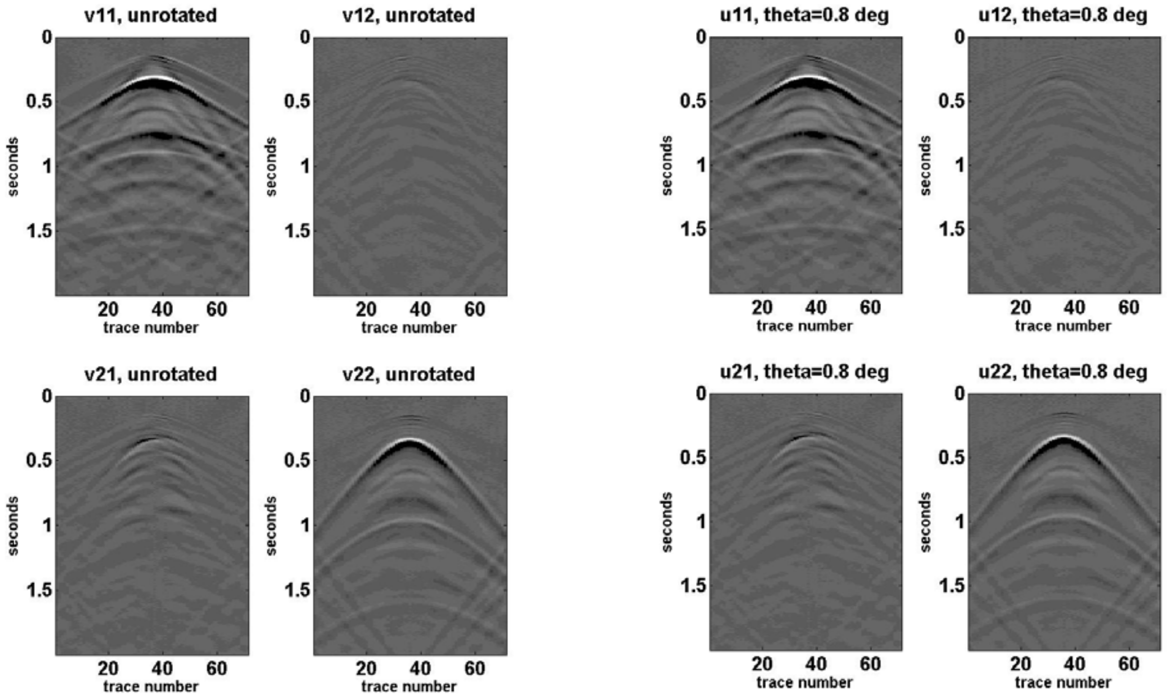

Fig. 18. 0°-azimuth shot gather acquired over the phenolic layer: 4 Horizontal components before rotation (left) and after rotation (right).

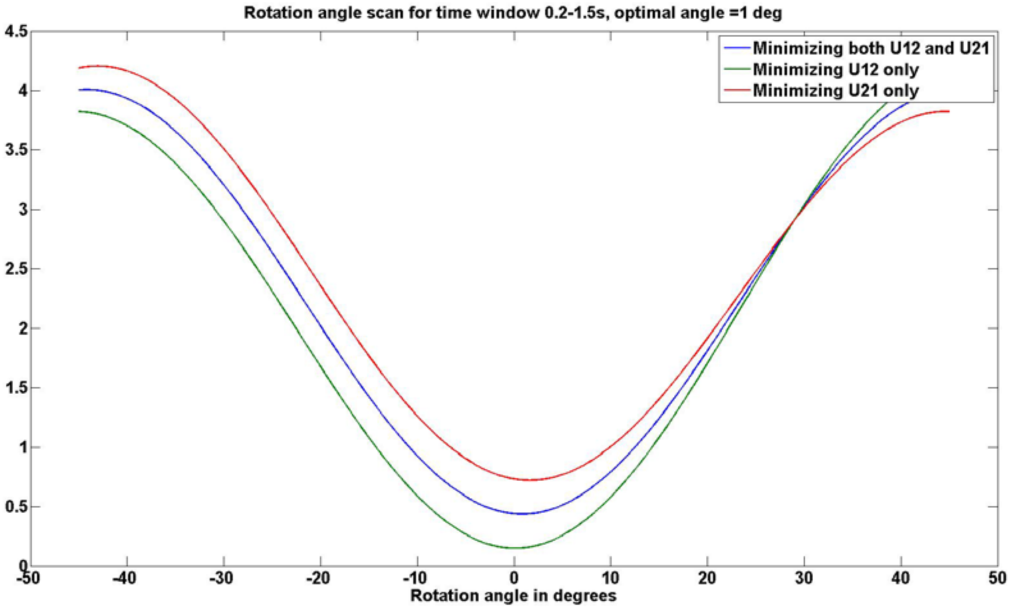

FIG. 19. 0°-azimuth shot gather: cross energy vs. rotation angle.

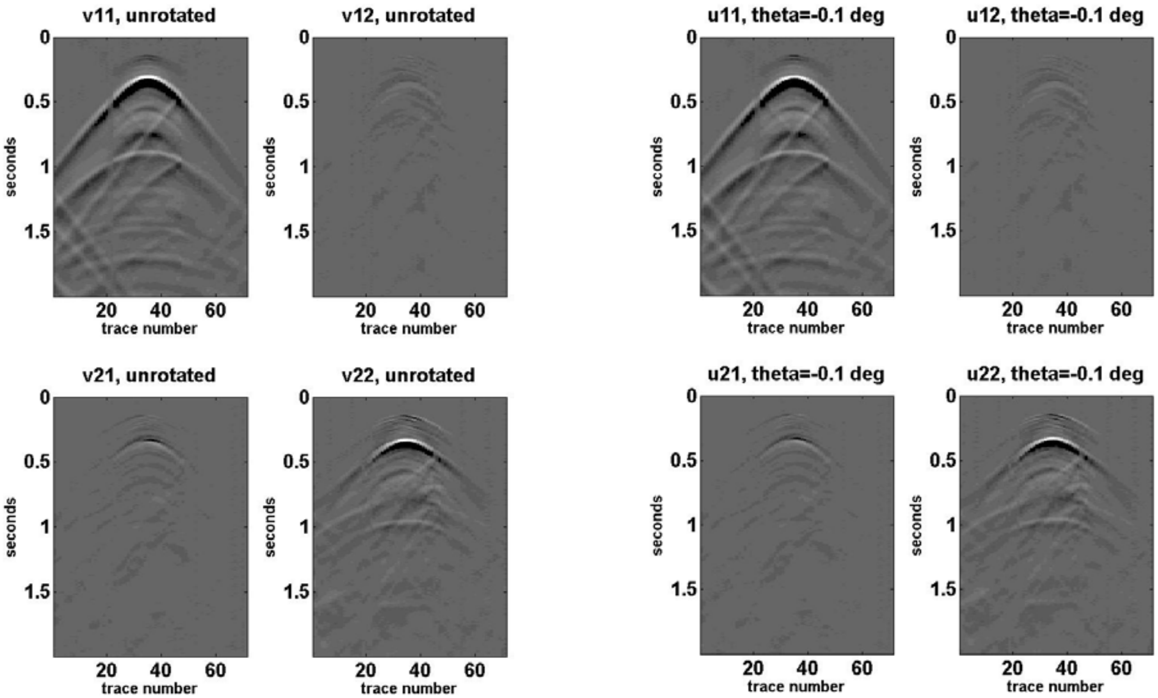

Fig. 20. 90°-azimuth shot gather acquired over the Phenolic layer: 4 Horizontal components before rotation (left) and after rotation (right).

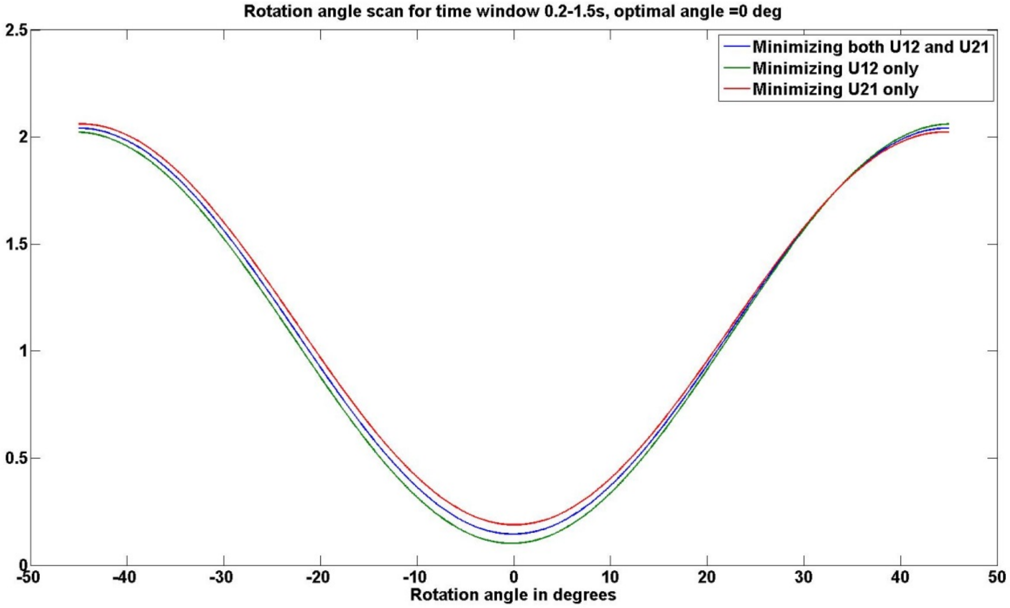

FIG. 21. 90°-azimuth shot gather: cross energy vs. rotation angle.

Using the second dataset, Alford rotation behavior is just as anticipated. The rotation angles are very small because acquisition coordinate system is similar to the natural coordinate system. The small angles are caused by small errors in acquisition. The results of Alford rotation for the second dataset are quite satisfying. They provide confidence in S-wave acquisition tools.

ESTIMATION OF ELASTIC STIFFNESS COEFFICIENTS

In anisotropic media, phase and group velocities are not equal. Group velocities at different angles of incidence (Θ) and azimuthal angles (Φ) can be easily measured in laboratory, as well in field. For orthorhombic media, Daley and Krebs (2006) have derived a relation between the P group velocity (V) and the density-normalized stiffness coefficients (A_{ij}):

$$\frac{1}{V^2(\vec{N})} \approx \frac{N_1^2}{A_{11}} + \frac{N_2^2}{A_{22}} + \frac{N_3^2}{A_{33}} - \frac{E_{23}N_2^2N_3^2}{A_{22}A_{33}} - \frac{E_{13}N_1^2N_3^2}{A_{11}A_{33}} - \frac{E_{12}N_1^2N_2^2}{A_{11}A_{22}}, \tag{11}$$

where

$$\vec{N} = (N_1, N_2, N_3) \tag{12}$$

$$N_1 = \sin(\Theta)\cos(\Phi) \tag{13}$$

$$N_2 = \sin(\Theta)\sin(\Phi) \tag{14}$$

$$N_3 = \cos(\Phi) \tag{15}$$

$$E_{23} = 2(A_{23} + 2A_{44}) - (A_{22} + A_{33}) \tag{16}$$

$$E_{13} = 2(A_{13} + 2A_{55}) - (A_{11} + A_{33}) \tag{17}$$

$$E_{12} = 2(A_{12} + 2A_{66}) - (A_{11} + A_{22}). \tag{18}$$

In the Phenolic medium, A_{11}, A_{22}, A_{33}, A_{44}, A_{55}, and A_{66} can be measured by estimating body wave (P and S) group velocities (V_{ij}) propagating along the x_j-axis and polarized along the x_i-axis as follows:

$$A_{11} = V_{11}^2 \tag{19}$$

$$A_{22} = V_{22}^2 \tag{20}$$

$$A_{33} = V_{33}^2 \tag{21}$$

$$A_{44} = V_{23}^2 = V_{32}^2 \tag{22}$$

$$A_{55} = V_{13}^2 = V_{31}^2 \tag{23}$$

$$A_{66} = V_{12}^2 = V_{21}^2 . \tag{24}$$

In the laboratory, $\sqrt{A_{44}}$, $\sqrt{A_{55}}$, and $\sqrt{A_{66}}$ *were* measured. $\sqrt{A_{33}}$ was measured too, but was assumed unknown in the inversion in order to use it to validate the results. Five stiffness coefficients (A_{11}, A_{22}, A_{33}, A_{12}, A_{13}, and A_{23}) are inverted for. For the inversion the second dataset, which has the acquisition explained by Fig. 4 and Fig 22 is used. That dataset consists of 3 common-shot gathers: one circular that has 200 m radius; and two linear at 0° and 90° azimuths. First P-wave arrival times (indicated by red on Fig. 23) are picked and used to calculate P group velocities by dividing distance between source and receiver over the time. Angles of incidence (Θ) and azimuthal angles (Φ) are calculated by trigonometric functions and shown in Fig 24. The circular gather has a wide range of azimuthal angles and a single angle of incidence that is approximately 24°. The line gathers have a single azimuthal angle 0° or 90° and a wide range of incidence angles.

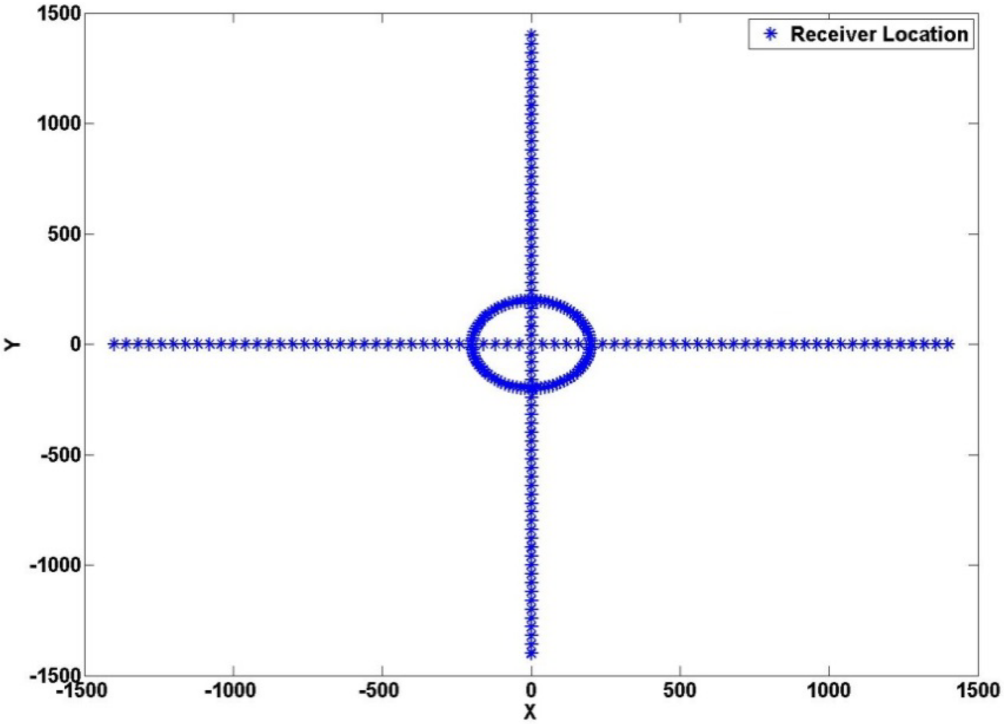

Fig. 22. Receiver locations on the top surface of the Phenolic.

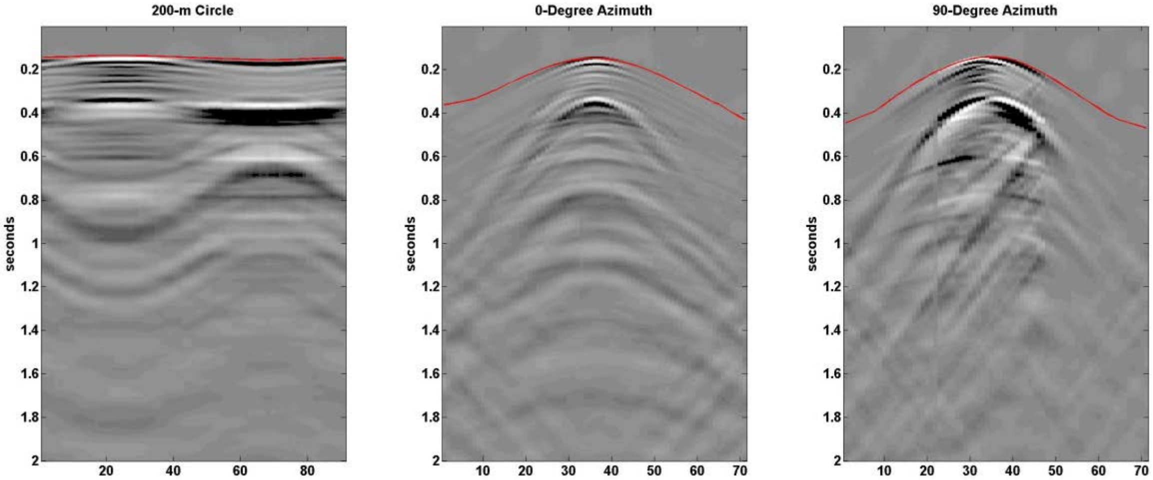

Fig. 23. Second dataset: one circular gather (left) that has 200 m radius; and two linear with 0^o (middle) and 90^o (right) azimuths. First P-wave arrivaltimes are indicated by red.

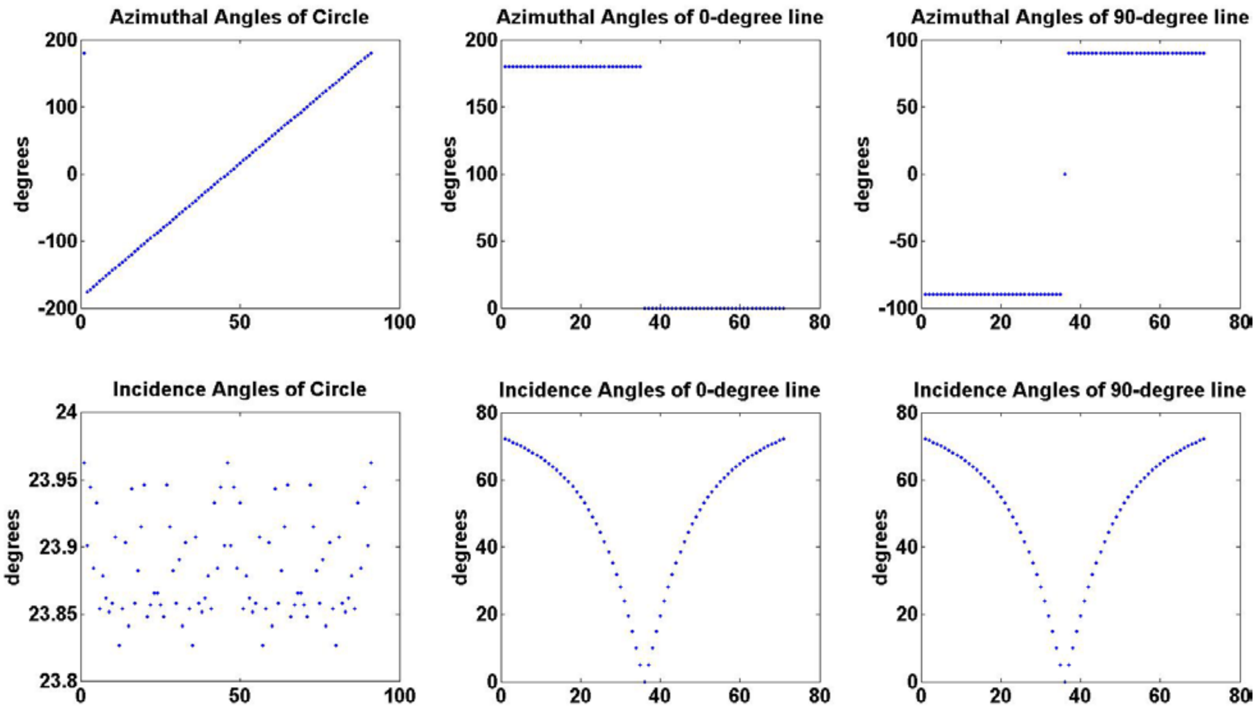

Fig. 24. Azimuthal and incidence angles of the three common-shot gathers. The circular gather has a wide range of azimuthal angles and a single angle of incidence that is approximately 24o. The linear gathers have a single azimuthal angle 0^{o} or 90^{o} and a wide range of incidence angles.

The P group velocity and stiffness coefficients relation, given by equation (11), can be rewritten in the form of

$$d = Gm \, , \tag{25}$$

where d is n-dimensional data vector, m is the 6-dimensionl model parameter vector, and G is the n-by-6 data kernel as:

$$\begin{bmatrix} \frac{1}{V_1^{\,2}} \\ \frac{1}{V_2^{\,2}} \\ \frac{1}{V_3^{\,2}} \\ \\ \\ \\ \frac{1}{V_n^{\,2}} \end{bmatrix} = \begin{bmatrix} N_{11}^2 & N_{21}^2 & N_{31}^2 & N_{21}^2N_{31}^2 & N_{11}^2N_{31}^2 & N_{11}^2N_{21}^2 \\ N_{12}^2 & N_{22}^2 & N_{32}^2 & N_{22}^2N_{32}^2 & N_{12}^2N_{32}^2 & N_{11}^2N_{22}^2 \\ N_{13}^2 & N_{23}^2 & N_{33}^2 & N_{23}^2N_{33}^2 & N_{13}^2N_{33}^2 & N_{13}^2N_{23}^2 \\ \\ \\ N_{1n}^2 & N_{2n}^2 & N_{3n}^2 & N_{2n}^2N_{3n}^2 & N_{1n}^2N_{3n}^2 & N_{1n}^2N_{2n}^2 \end{bmatrix} \begin{bmatrix} \frac{1}{A_{11}} \\ \frac{1}{A_{22}} \\ \frac{1}{A_{33}} \\ -\frac{E_{23}}{A_{22}A_{33}} \\ -\frac{E_{13}}{A_{11}A_{33}} \\ -\frac{E_{12}}{A_{11}A_{22}} \end{bmatrix} \tag{26}$$

The linear problem is solved for model parameter vector (*m*). The first three elements of the model parameter vector can provide us with A_{11}, A_{22}, and A_{33}. In the laboratory, V_{13} is measured by measuring the group velocity of S wave that propagates along the x_3-axis and polarized along the x_1-axis and found to be 1562.5 m/s. Similarly, V_{21} and V_{23} were measured and found to be 1785.7 m/s and 1451.6 m/s. Therefore, A_{44}, A_{55}, and A_{66} can be calculated using equations (22), (23), and (24). Hence, the last three elements of the model parameter vector can provide us with A_{23}, A_{13}, and A_{12}. Three measured coefficients and six inverted coefficients from the density-normalized stiffness coefficients of the Phenolic layer in (m^2/s^2) are as follows:

$$A_{ij} = \begin{bmatrix} 1.3280e+07 & 1.0946e+07 & 4.9801e+06 & 0 & 0 & 0 \\ 1.0946e+07 & 8.7328e+06 & 6.2308e+06 & 0 & 0 & 0 \\ 4.9801e+06 & 6.2308e+06 & 1.1114e+07 & 0 & 0 & 0 \\ 0 & 0 & 0 & 2.1072e+06 & 0 & 0 \\ 0 & 0 & 0 & 0 & 2.4414e+06 & 0 \\ 0 & 0 & 0 & 0 & 0 & 3.1888e+06 \end{bmatrix} \tag{27}$$

From equation (21), V_{33} can also be calculated from the inverted A_{33}. It is equal to 3333.7 m/s. In the laboratory, V_{33} was measured too by measuring the group velocity of P wave that propagates along the x_3-axis and polarized along the x_3-axis and found to be 3358.2 m/s. The error between measured and calculated V_{33} is very small and equal to 0.73%. Table 2 summarizes body wave group velocities (V_{ij}) in the Phenolic. The resolution matrix (*N*) measures how well the data kernel resolves the model parameter. It is calculated by

$$N = GG^{-1} \tag{28}$$

and is shown in Fig. 25. for the three common-shot gathers together. The resolution matrix for each gather is shown by Fig. 26. The resolution matrix of all gathers and the one of the circular gather resolve the model parameter well. On the other hand the resolution matrix of each azimuthal line does not resolve the model parameter well, but the combination of both lines does.

V_{11}	V_{22}	V_{33}	V_{23}	V_{13}	V_{12}
3644.1	2955.1	3333.7	1451.6	1562.5	1785.7

Table 2. Body wave velocities (V_{ij}) that propagates along x_i-axis and polarized along x_j-axis in (m/s).

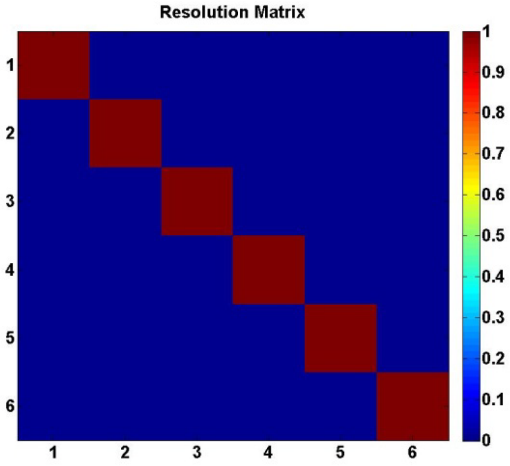

Fig. 25. The resolution matrix of all gathers: one circle and two lines.

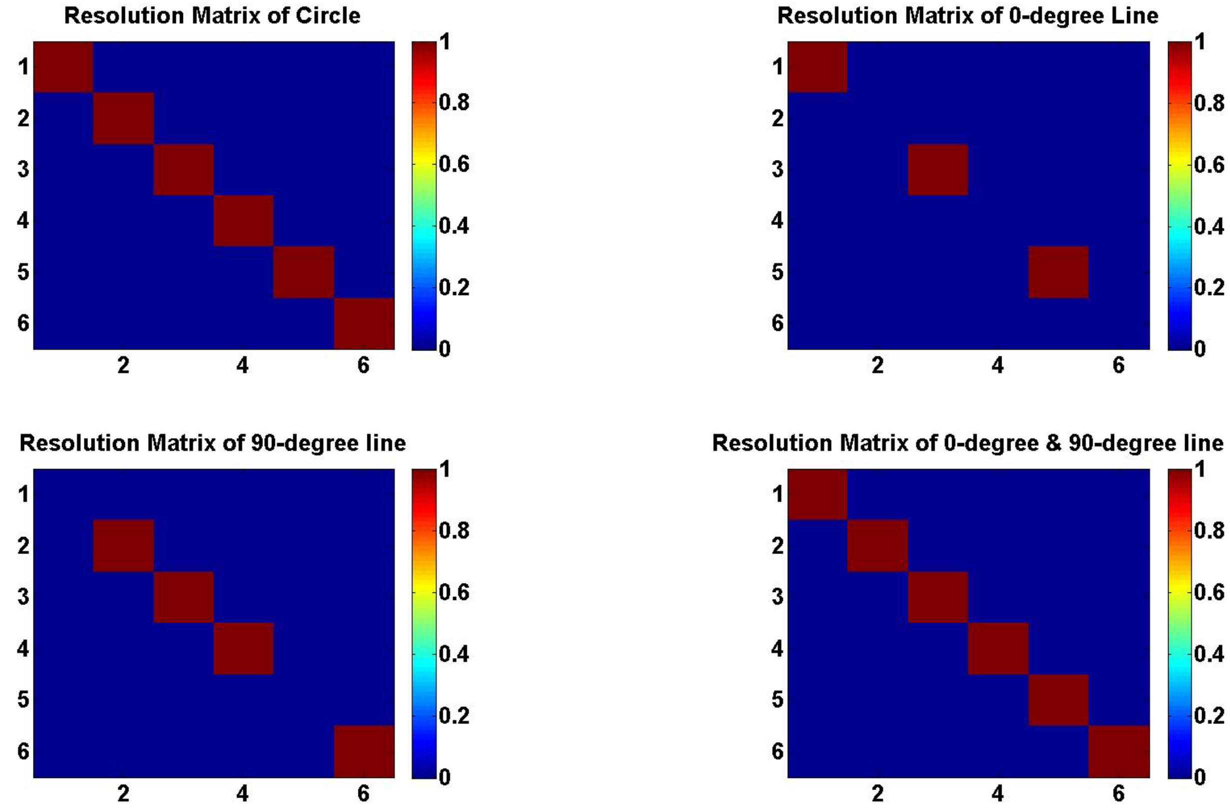

Fig. 26. The resolution matrix of: one circle (top left), 0° line (top right), 90° line (bottom left), and both lines (bottom right).

CONCLUSIONS

Physical modeling is a valuable tool that can assist in the evaluation and development of practices for fracture characterization. This report has utilized physical modeling, and in summary:

- A physical model was constructed in the laboratory to represent a vertically-fractured reservoir overlaid by isotropic overburden. This model was used to acquire the first dataset. The second data set was acquired over a single Phenolic layer

- The first dataset consists of three common-receiver gathers were acquired over the 2-layer model; each has a constant offset (***r*** = 250 m, 500 m and 1000 m) and variant azimuth angles (0^0- 360^o).

- Fracture plane orientation was easily identified from the third common-receiver gather (***r*** = 1000 m) by P-wave first-arrival times. Elliptical fitting of P-wave first-arrival times was employed to identify the fracture plane orientation from the three common-receiver gather.

- An Alford rotation was applied to dataset that was acquired over 2-layer model to transform the data from acquisition system coordinate to natural system coordinate. Results of Alford analysis were not as anticipated and that was the motivation to acquire the second dataset.

- The second dataset consists of one circular gather which has 200 m radius and two linear gathers with 0^o and 90^o azimuths acquired over the anisotropic medium.

- Alford rotational analysis was applied to the second dataset. The results of Alford rotation for the second dataset are quite satisfying because they provide confidence in S-wave acquisition tools.

- Second dataset was used to invert for the elastic stiffness coefficients of the Phenolic medium over which it was acquired.

ACKNOWLEDGMENT

We thank the sponsors of CREWES for their support. We also gratefully acknowledge support from NSERC (Natural Science and Engineering Research Council of Canada) through the grant CRDPJ 379744-08. The main author thanks Dr. Pat Daley for reviewing this report. He is grateful to Saudi Aramco for PhD studies sponsorship.

REFERENCES

Al Dulaijan, K., Owusu, J. C., & Weber, D. C., 2012, Azimuthal anisotropy analysis of walkaround vertical seismic profiling vertical seismic profiling: a case study from Saudi Arabia. Geophysical Prospecting, 60(6), 1082-1094.

Alford, R. M., 1986, Shear data in the presence of azimuthal anisotropy: Dilley Texas, SEG Expanded Abstracts, SEG Annual Convention.

Crampin, S., 1981, A review of wave motion in anisotropic and cracked elastic-media. Wave motion, 3(4), 343-391.

Daley, P. F., and E. S. Krebes, 2006, Quasi-compressional group velocity approximation in a weakly anisotropic orthorhombic medium: Journal of Seismic Exploration, 14, 319–334.

Mahmoudian, F., 2013, Physical Modeling and Analysis of Seismic Data from a Simulated Fractured Medium: Ph.D. thesis, University of Calgary.

Mah, M., 1999, Experimental determination of the elastic coefficients of anisot ropic materials with the slant-stack method: Ph.D thesis: University of Alberta.

Mahmoudian, F., & Margrave, G. F., 2013, AVAZ Inversion for Fracture Orientation and Intensity-A Physical Modeling Study. In 75th EAGE Conference & Exhibition incorporating SPE EUROPEC 2013.

Mahmoudian, F., Margrave, G., Daley, P., Wong, J., and Henley, D., 2014, Estimation of elastic stiffness coefficients of an orthorhombic physical model using group velocity analysis on transmission data. Geophysics, 79, R27–R39.

Musgrave, M. J. P., 1970. Crystal acoustics: Introduction to the study of elastic waves and vibrations in crystals. San Francisco: Holden-Day.

Thomsen, L., 1986, Weak elastic anisotropy. Geophysics, 51, 1954–1966.

Vestrum, R. W., 1994, Group- and phase-velocity inversions for the general anisotropic stiffness tensor: M.S. thesis, University of Calgary.

Winterstein, D., 1992, How shear-wave properties relate to rock fractures: Simple cases. The Leading Edge, 11(9), 21-28.

Wong, J., F. Mahmoudian, and G. Margrave, 2011, Physical modeling III: Acquiring modeled data for VVAZ/AVAZ analysis: CREWES Research Report, 23, 1–17.